ARTICLE

Encapsulation of Red Phosphorus in Carbon Nanocages with Ultrahigh Content for High-Capacity and Long Cycle Life Sodium-Ion Batteries

Weili Liu, Lingyu Du, Shunlong Ju, Xueyi Cheng, Qiang Wu, Zheng Hu,* and Xuebin Yu*

Read Online

ACCESS | Metrics & More | Article Recommendations | SI Supporting Information

ABSTRACT: Red phosphorus (RP) has attracted great attention as a potential candidate for anode materials of high-energy density sodium-ion batteries (NIBs) due to its high theoretical capacity, appropriate working voltage, and natural abundance. However, the low electrical conductance and huge volumetric variation during the sodiation−desodiation process, causing poor rate performance and cyclability, have limited the practical application of RP in NIBs. Herein, we report a rational strategy to resolve these issues by encapsulating nanoscaled RP into conductive and networked carbon nanocages (denoted as RP@ CNCs) using a combination of a phosphorus-amine based method and evacuation-filling process. The large interior cavities volume of CNCs and controllable solution-based method enable the ultrahigh RP loading amount (85.3 wt %) in the RP@ CNC composite. Benefiting from the synergic effects of the interior cavities and conductive network, which afford high structure stability and rapid electron transport, the RP@CNC composite presents a high systematic capacity of 1363 mA h g^{-1} at a current density of 100 mA g^{-1} after 150 cycles, favorable high-rate capability, and splendid long-cycling performance with capacity retention over 80% after 1300 cycles at 5000 mA g^{-1}. This prototypical design promises an efficient solution to maximize RP loading as well as to boost the electrochemical performance of RP-based anodes.

KEYWORDS: *red phosphorus, carbon nanocages, high loading ratio, high systematic capacity, sodium-ion battery*
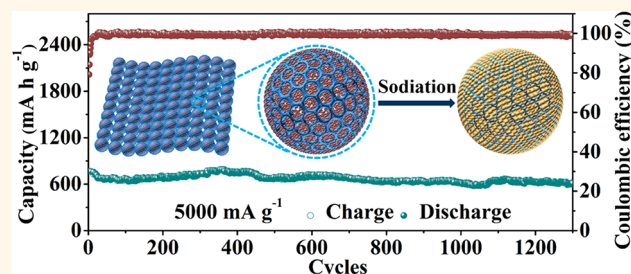
Among the advanced battery technologies in the era of post-lithium-ion batteries, sodium-ion batteries (NIBs) have been recognized as priority alternatives to store clean energy due to their merits of low cost and abundance.[1−3] Currently, a wide range of cathodes have been reported for NIBs; nevertheless, development of viable anode materials is still the main scientific challenge for a competitive NIB technology.[4−6] Red phosphorus (RP) has emerged as a potential anode material for NIB because it is abundant, commercially available, and has much higher theoretical capacity (2595 mA h g^{-1} with Na$_3$P) than all the available anode materials for NIBs at present.[7−11] Nevertheless, the practical application of RP as an anode material for NIBs is still impeded by its poor electrical conductivity (∼10^{-4} S cm^{-1}) and huge volume variation (>490%) during the sodiation−desodiation process, which causes limited rate and cycling performance.[7,8]

To tackle these barriers, an efficient strategy is to integrate RP with carbon-based conductive matrixes[7,8,12−31] (*e.g.*, super P carbon,[7] carbon black,[8] graphene,[12−19] carbon nano-

tubes,[20−23] porous carbon,[24−27] and so forth[28−31]). It was reported that these carbon materials could synergistically boost the electronic conductivity and accommodate the volume variation of RP. For example, Liu *et al.* designed and synthesized equidistributed honeycomb-like hierarchical micromesoporous carbon nanospheres (HHPCNSs) with high pore volume to load RP. The large pore volume provided sufficient void space for the expansion of RP and the honeycomb-like carbon network offer high electronic conductivity for RP, thus giving the HHPCNSs/P composite high capacity, splendid rate performance, and excellent cycling stability.[27] In general, ball-milling is a facile and effective
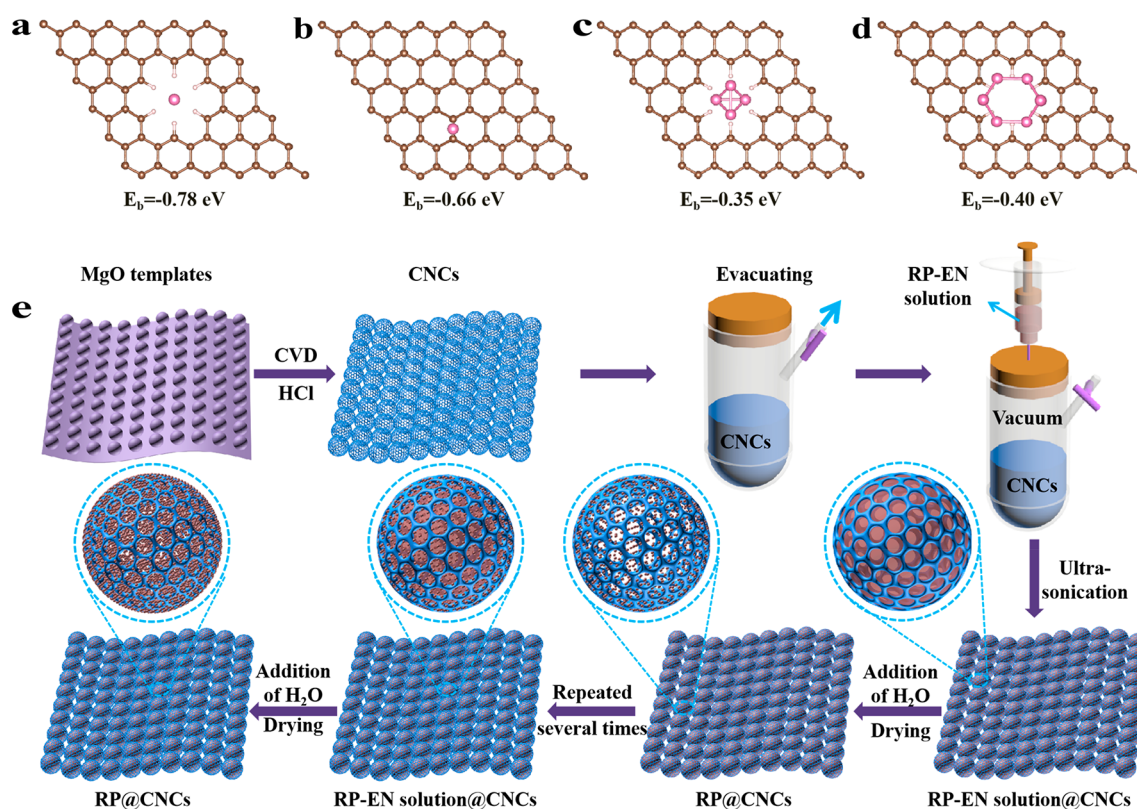
Figure 1. Configurations and corresponding calculated bonding energy of P atom on graphitic layer (a) with and (b) without a micropore. Configurations and corresponding calculated bonding energy of (c) P_4 and (d) P_8 cluster on graphitic layer with a micropore during the growth process of P_n cluster. In the models, the carbon (C), hydrogen (H), and phosphorus (P) elements are displayed as spheres in brown, light pink, and hot pink, respectively. (e) Schematic drawing for the synthesis of RP@CNC composite.

method to fabricate RP−carbon anodes by hybridizing RP with carbon-based matrixes,[7,8,12,21] in which the RP contents in the RP−carbon hybrids are easy to control and a high mass ratio of 70 wt % RP is usually employed.[7,8,12,21] However, simply mixing RP with carbon matrixes *via* ball-milling inevitably triggers nonuniform particle size and limited contact between carbon-based matrixes and RP, which cannot efficiently buffer the huge volume variation, or suppress the agglomeration and detachment of RP during the cycling. As a result, the long-term stability still remain an issue for ball-milled RP−carbon anodes.[9,11,14]

Another conventional method for the preparation of RP−carbon anodes is vaporization−-condensation, which can attach RP on carbon materials and endow RP anodes with enhanced reactivity and electronic conductivity. This vaporization−condensation strategy has been demonstrated to effectively improve the long-term cycling stability.[13,16,19,20,23,25−27,30] Liu *et al.* prepared red-phosphorus-impregnated carbon nanofibers and demonstrated the encapsulation strategy to effectively boost the electrochemical property, delivering ∼1850 mA h g^{-1} over 500 cycles at 0.1 A g^{-1} and >1000 mA h g^{-1} over 5000 cycles at 1 A g^{-1}.[30] Nevertheless, for the vaporization−condensation technique, the distribution and loading amount of RP in the carbonaceous matrixes are uncontrollable.[9,14]

Recently, our group developed a phosphorus−amine-based method to realize uniform distribution and controllable loading amount of nanoscale RP (NRP) on the reduced graphene oxide (rGO).[19] The obtained NRP−rGO composite with optimal loading radio (56.3 wt %) exhibited excellent electrochemical performance including high reversible capacity and stable long-term cyclability. However, with the increase of the loading ratio of NRP, the ultrafine NRP overlapped and aggregated on the rGO, which cannot sustain the volume variation over the discharge/charge process, causing fast capacity decay. Therefore, there is a crucial requirement to develop advanced carbon host structures which can ensure a high RP loading amount and simultaneously encapsulate RP within them to effectively withstand the volumetric variation of RP during cycling.

In recent years, carbon nanocages (CNCs) as one branch of carbon-based materials with increasing attraction have become a multifunctional and advanced energy storage platform, owing to their large surface area, big interior cavities with abundant subnanometer microchannels across the shells, as well as the available hierarchical porous architecture and high conductivity.[32−39] These characteristics, especially the big interior cavities and conductive networks, enable the CNCs to be ideal hosts for RP encapsulation, which may afford high RP loading, rapid electron transport, and enough volume expansion accommodation. In this work, based on the results of first theoretical simulations, which reveal that the micropores with edges in CNCs favor the nucleation and growth of P_n clusters by micropore trapping of [ethylenediamine-P_n]$^-$ (denoted as [EN-P_n]$^-$), followed by the spontaneous deethylenediamine, nanoscaled RP was successfully encapsulated into conductive and networked CNCs (denoted as RP@CNCs) through a combination of a facile phosphorus−amine based method and evacuation-filling process. The optimal RP@CNC composite possesses an ultrahigh RP loading
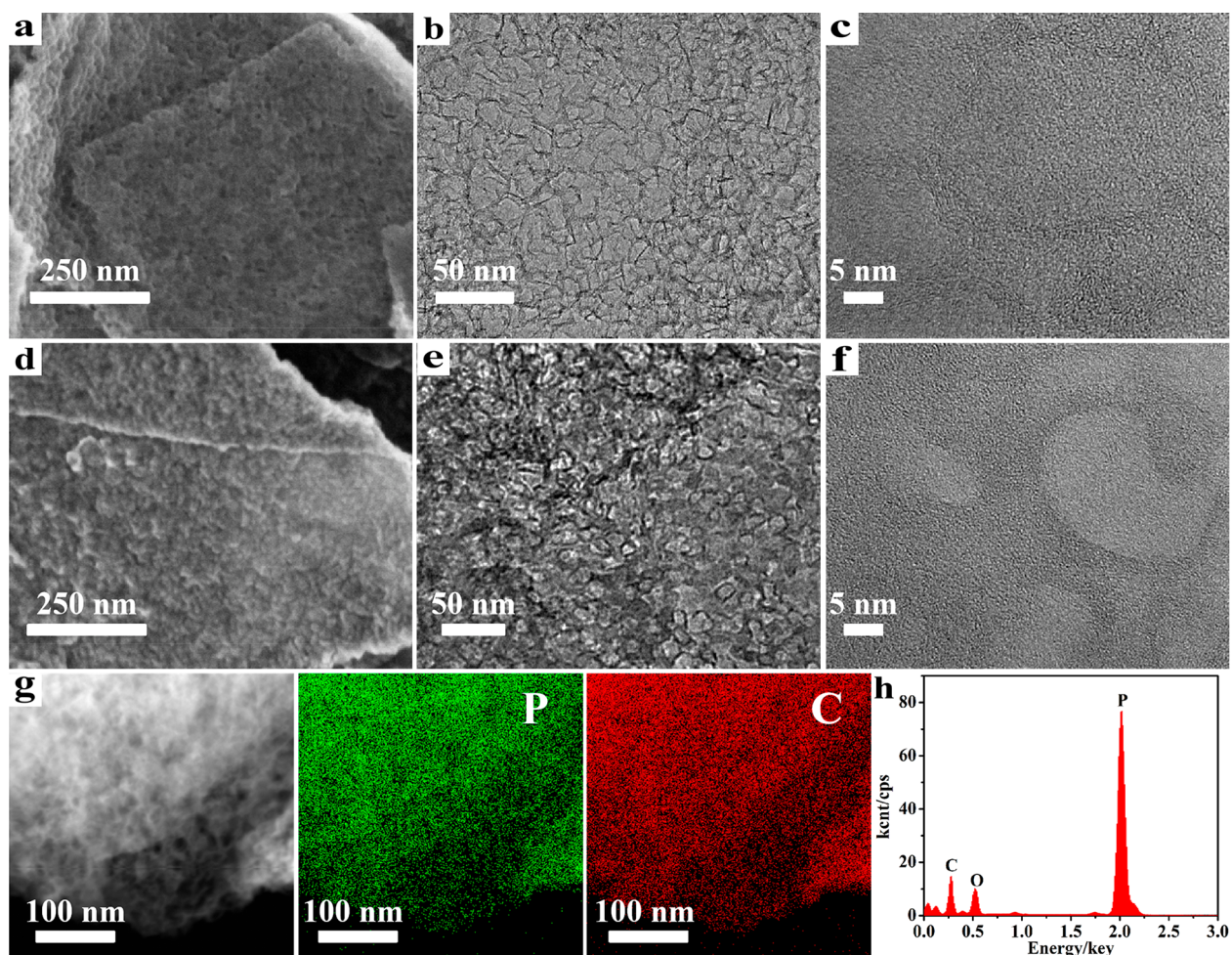
Figure 2. (a) SEM, (b) TEM, and (c) HRTEM images of CNCs; (d) SEM, (e) TEM, and (f) HRTEM images of RP@CNC composite. (g) Dark-field STEM image and corresponding elemental mapping. (h) EDS spectrum for RP@CNCs composite.

amount of 85.3 wt % and simultaneously displays impressive sodium storage performance, including high specific capacity of 1363 mA h g^{-1} at a current density of 100 mA g^{-1} over 150 cycles, superior high-rate capability, and stable long cyclic life with capacity of 610 mA h g^{-1} after 1300 cycles at 5000 mA g^{-1}.

RESULTS AND DISCUSSION

It has been revealed that the CNCs have many micropores and the micropores with edges are favorable for trapping anions.[36,39] These abundant micropores across the shells of CNCs may facilitate the infiltration of RP-EN complex solution as well as trapping [EN-P$_n$]$^-$ anions. We first studied the effect of micropores on the nucleation and growth of P$_n$ clusters using P, P$_4$, P$_8$, and the graphitic layer with or without a micropore as model compounds by first-principles calculations (Figure 1a−d). For the CNCs, the P is nucleated in the micropore with an adsorption energy of −0.78 eV, higher than −0.66 eV for the case of carbon layer without micropore (Figure 1a,b). When the P in the micropore is growing up to P$_4$ and P$_8$, respectively, the binding energies are −0.35 and −0.40 eV, respectively (Figure 1c,d). These results indicate that the micropores of CNCs are more favorable for the nucleation and growth of P$_n$ clusters. Therefore, the P$_n$ clusters would nucleate at the micropore sites and gradually

grew from around to center in the interior cavities, which are beneficial to the loading of RP with high ratio.

On the basis of the above-mentioned prediction, the RP@ CNC composite was synthesized through a combination of a facile phosphorus−amine-based method and evacuation-filling process, using CNCs with micropores as the hosts. The synthetic process is schematically illustrated in Figure 1e. The connected CNCs with interior cavities were prepared by a chemical vapor deposition method using MgO as templates, according to the previous work.[34−36] After the removal of MgO templates, the connected CNCs were filled with RP−EN complex solution (Figure S1a) through subnanometer microchannels across the shells under the condition of evacuation and ultrasonication.[40,41] Then RP particles precipitated from the RP−EN complex solution (Figure S1b) with the addition of deionized water. After removing the solvents, RP particles were finally encapsulated in CNCs. To realize the maximum loading of RP, the processes were repeated for several times.

We first examined the morphology and detailed microstructure of the CNCs using scanning electron microscopy (SEM) and transmission electron microscopy (TEM). As shown in Figure 2a and Figure S2a,b, the obtained CNCs present sheetlike morphology with porous surface. The size of the nanosheets is several microns, and the thickness is 30−40 nm (Figure S2a,b). In the nanosheets, abundant hollow interior cavities (10−30 nm) surrounded by thin low
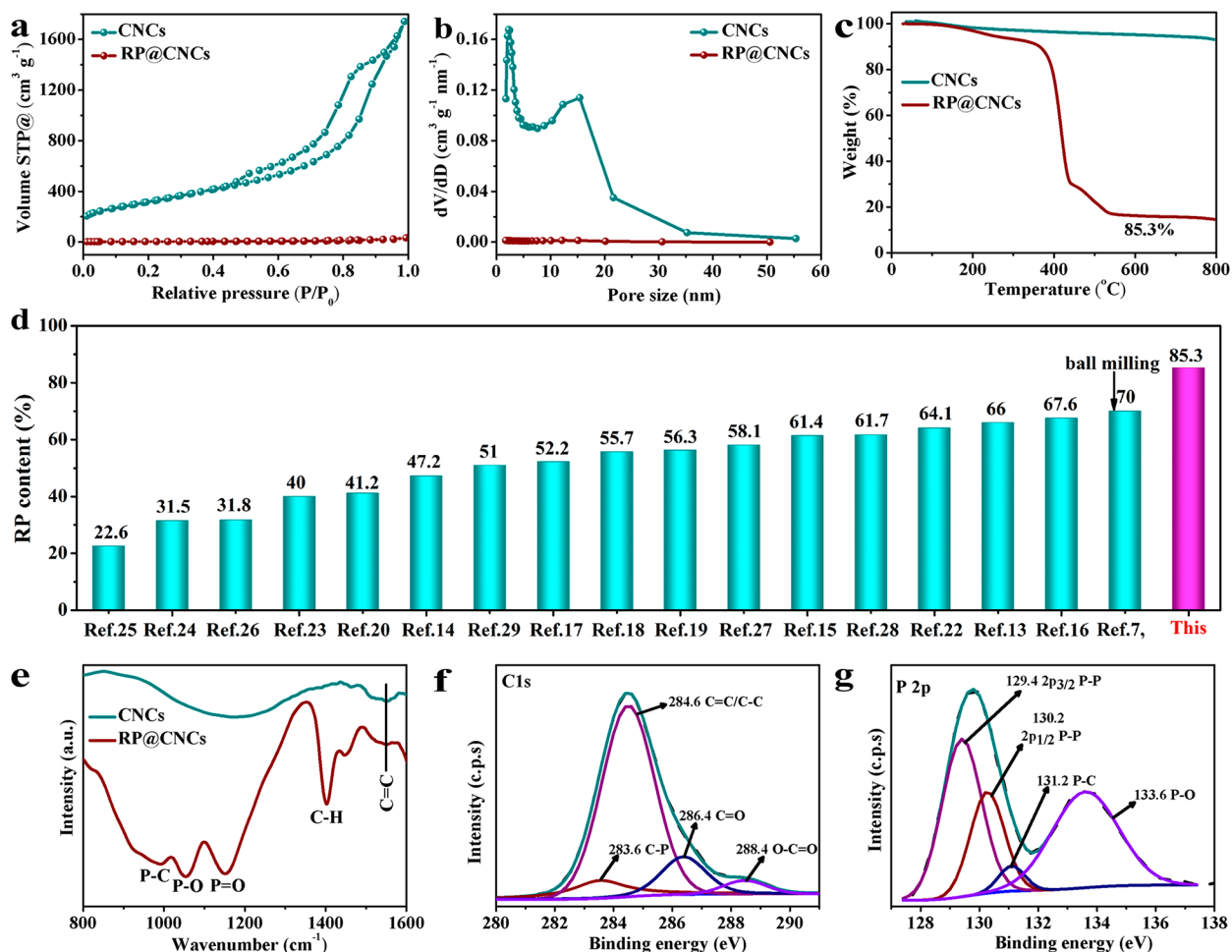
Figure 3. (a) N_2 adsorption/desorption isotherms and (b) pore size distribution plots of CNCs and RP@CNCs. (c) TGA curves of CNCs and RP@CNCs. (d) Comparison of RP loading in several RP-based composites reported recently for NIBs. (e) FTIR spectra of the CNCs and the RP@CNC composite. High-resolution (f) C 1s and (g) P 2p spectra of the RP@CNC composite.

graphitized carbon shells are interconnected with each other (Figure 2b,c and Figure S3a,b), forming a conductive network. The interior cavities contribute to the high dispersion of RP particles and accommodate the volume change during cycling. The nitrogen absorption−desorption isotherm (Figure 3a,b) shows that the CNCs possess a large specific surface area ($1146 \ m^2 \ g^{-1}$) and a high pore volume ($2.695 \ cm^3 \ g^{-1}$) with a mean pore diameter of ∼15 nm, which guarantee the high loading ratio of RP. The peak at ca. 2 nm is originated from the microchannels across the low graphitized carbon shells, confirming the unsealed feature around the big interior cavities (Figure 3b), which are beneficial to the nucleation of P_n clusters and the infiltration of solution. In addition, this architecture is also beneficial to the structural stability, *e.g.*, refraining the CNCs from agglomerate or restack together due to the intrinsic van der Waals interaction.[42]

The obtained RP@CNC composite keeps the layered structure without exposed agglomeration of RP on the surface (Figure 2d and Figure S2c,d). The TEM and high-resolution TEM (HRTEM) images of RP@CNCs reveal that the hollow interior cavities in the CNCs are partially filled, attributed to the RP encapsulation (Figure 2e,f and Figure S3c,d). The Brunauer−Emmett−Teller (BET) specific surface area dropped to $13.1 \ m^2 \ g^{-1}$ and the pore volume decreased to $0.049 \ cm^3 \ g^{-1}$ (Figure 3a, b), confirming that the RP was successfully

entrapped in the interior cavities. The related elemental mapping of carbon and phosphorus further demonstrate the homogeneous distribution of RP in the CNCs (Figure 2g). The energy dispersive X-ray spectroscopy (EDS) spectrum of the RP@CNC composite shows a strong P peak and a weak C peak (Figure 2h), giving a high phosphorus content of 83.6 wt %. The existence of O in the EDS spectrum is due to the oxidation of the composite during measurement, which results in a slight decrease of phosphorus content. The content of RP in the RP@CNC composite was determined to be 85.3 wt % by the thermogravimetric analysis (TGA) (Figure 3c), which is higher than that of any other RP−carbon composite as an anode for NIBs reported so far (Figure 3d).[7,8,12−29]

Parts a and b of Figure S4 display the X-ray diffraction (XRD) patterns and Raman spectra of the CNC and RP@CNC composite. The broad peak at $2\theta \approx 25°$ in the XRD pattern for CNCs is related to low graphitized carbonaceous materials (Figure S4a),[25,26] consistent with the result of its Raman spectrum (Figure S4b). After encapsulating RP into the CNCs, the RP@CNC composite shows almost no characteristic peaks of RP in the XRD pattern and Raman spectrum (Figure S4a,b), primarily due to the downsizing of RP encapsulated in interior cavities between 10 and 30 nm and its amorphous state when nanoconfined in CNCs. All of the results including SEM, TEM, XRD, and Raman confirmed the
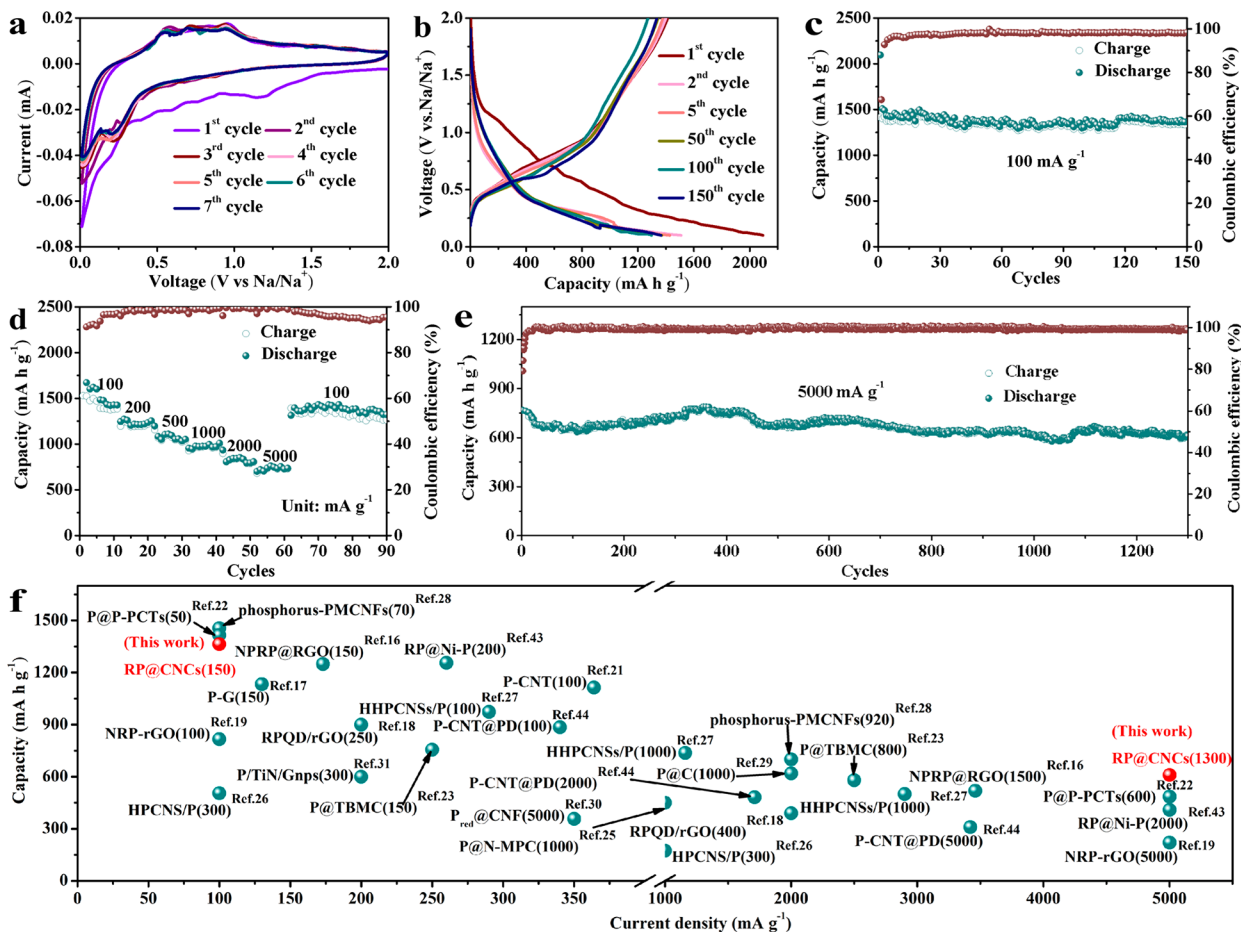
Figure 4. Electrochemical properties of the RP@CNC composite. (a) CV profiles of the RP@CNC composite at a scan rate of 0.1 mV s^{-1}. (b) GDC profiles and (c) cyclic performance of the RP@CNC composite anode in the voltage range from 0.1 to 2.0 V at 100 mA g^{-1}. (d) Rate capability at various current densities (100–5000 mA g^{-1}) and (e) long-term cyclic property at 5000 mA g^{-1} for 1300 cycles of the RP@CNC composite electrode. (f) Cycling performance of the RP@CNC electrode compared with some reported RP-based NIB anodes (the number in parentheses for every electrode is the number of cycles).

fact that RP was mostly encapsulated in the interior cavities with the minor RP layer deposited on the external surface of CNCs. To examine the detailed form of RP in the RP@CNC composite, Fourier transform-infrared spectroscopy (FTIR) and X-ray photoelectron spectroscopy (XPS) measurements were performed. Figure 3e presents the FTIR characteristic peak of the RP@CNC composite at 991, 1151, and 1053 cm^{-1}, respectively, corresponding to the P–C,[43,44] P=O, and P–O bonds.[43] Additionally, the characteristic peaks of C=C (1550 cm^{-1}) and C–H (1400 cm^{-1}) confirm the existence of CNCs.[45] The XPS results give similar conclusions. The C 1s spectra in Figure 3f was fitted with typical bonds of O–C=O (288.4 eV), C=O (286.4 eV), C=C/C–C (284.6 eV) from CNCs and chemical bond of C–P (283.6 eV) between RP and CNCs,[16] which suggested lots of oxygen-containing functional groups and abundant defects in the CNCs. These active sites and edges are favorable for the nucleation and growth of P$_n$ clusters (Figure 1a–d). The high oxygen content of CNCs, which indicates a large amount of active sites and edges, can restrain the aggregation of RP and guarantee a great quantity of ultrasmall RP nanoparticles to be evenly confined, thus improving the electrochemical property of the RP@CNC composite effectively.[20] Figure 3g shows the P 2p spectra, which were fitted into four peaks at 133.6, 131.2, 130.2, and 129.4 eV, confirming the existence of P–O, P–C, 2p1/2 P–P,

and 2p3/2 P–P bonds.[46–48] The presence of C–P or P–C bonds is consistent with the first-principles calculations in Figure 1a–d.

The RP@CNC composite was then evaluated as an anode material in a half-cell of NIBs. Figure 4a presents the cyclic voltammetry (CV) curves of the first seven cycles at a sweep rate of 0.1 mV s^{-1} in the voltage range of 0.01–2.0 V *versus* Na$^+$/Na. It can be seen that different from the subsequent cathodic scans, the first cathodic scan curve has two reduction peaks. The peak at about 1.14 V corresponds to the irreversible decomposition of electrolyte to generate solid electrolyte interphase (SEI) films,[26,49] and another peak at ~0.19 V is originated from the sodiation of RP to produce Na$_x$P compounds, acting as an activation process.[25] Subsequently, the peak position progressively moves toward a higher voltage (~0.21 V) during the following cathodic scans, indicating the decreased polarization. In the reversed anodic scans, it can be observed that three oxidative peaks are centered at 0.58, 0.72, and 0.93 V, respectively, revealing the stepwise desodiation process.[7,8,20] For the subsequent series of anodic–cathodic scans, the peak positions and peak areas remain stable after the activation of the first cathodic scan, indicating stable cyclability and high reversibility of the RP@CNC anode. As a comparison, the CV of CNCs was also measured to investigate the influence of CNCs on the RP@CNC composite (Figure
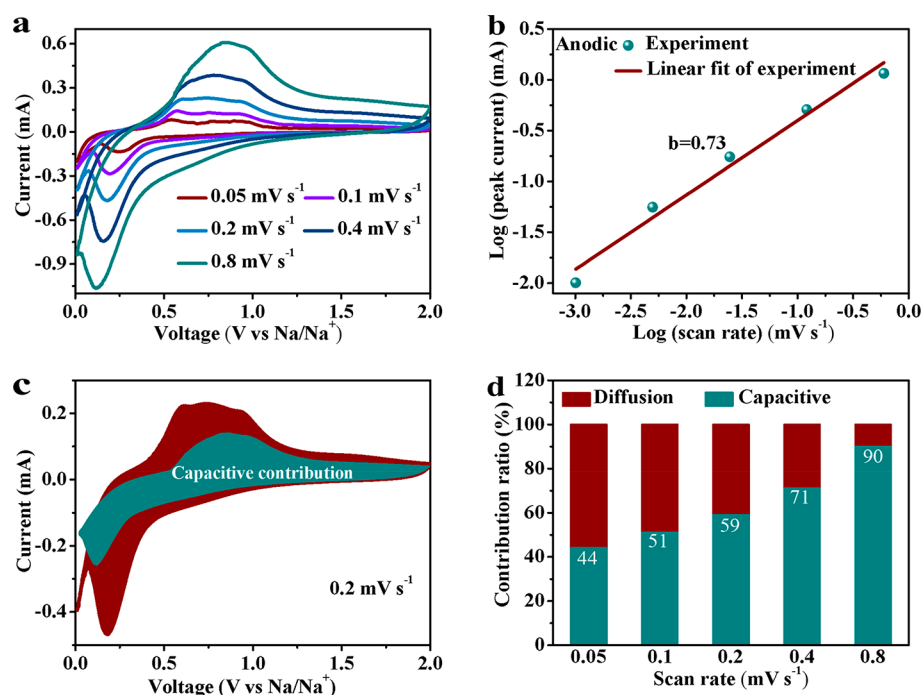
Figure 5. Kinetics analysis of RP@CNC composite for NIBs. (a) CV profiles at variety of scan rates, (b) relationship between log (peak current) and log (scan rate), (c) capacitive and diffusion contribution separated at a scan rate of 0.2 mV s^{-1}, and (d) capacitive contribution ratio at different scan rates.

S5a). The results show that the curves of CNCs have only one reduction peak in the region of 1.0−1.5 V during first cathodic scan, which is related to the generation of insoluble SEI film.[26,49] Similar results are shown in the galvanostatic charge–discharge (GDC) profiles of CNCs (Figure S5b), which presents only one voltage plateau in the first discharge curve. The ultralarge SEI film area, which contributes to the large irreversible loss of capacity, should be associated with the overlarge specific surface area of CNCs. However, it disappears in the RP@CNC composite (Figure 4a,b), which is due to the occupation of RP in the micropore of CNCs, thus reducing the specific surface area (Figure 3a,b). The GDC profiles of the RP@CNC electrode at 100 mA g^{-1} are shown in Figure 4b, which show typical features of RP electrodes and consistent results with CV. The discharge plateaus below 0.5 V are the characteristic of the sodiation. In the charge profiles, there are three potential plateaus centered at around 0.5, 0.7, and 0.9 V, respectively, which resulted from the stepwise desodiation process. From the second cycle to 150th cycle, the GDC profiles are almost overlapped with decreasing polarization, implying the outstanding reversibility and excellent stability of RP@CNC electrode.

Thereafter, the cycling ability and rate performance of RP@CNC electrode are elucidated. Notably, the specific capacities are calculated according to the mass of the RP@CNC composite. As shown in Figure 4c, the RP@CNC composite presents a reversible capacity of 1414 mA h g^{-1} in the first cycle and an initial Coulombic efficiency (ICE) of 67.5%. The irreversible loss of capacity during the first discharge/charge process is primarily resulted from the formation of SEI film and low ICE (about 13%) of the CNCs (Figures S5b and S7a). After 150 cycles, the RP@CNC composite still maintains a high reversible capacity of 1363 mA h g^{-1}, indicating its outstanding cyclic stability. From the 10th cycle, the Coulombic efficiency almost stabilizes at 97%, indicating the

high reversibility of the RP@CNC composite. The lower Coulombic efficiency at low current density in Figure 4c is attributed to the fact that the RP@CNC composite reacts with sodium more fully at low current density, which leads to more severe pulverization, thus resulting in poor reversibility.[51] In addition, the RP@CNC anode also exhibits a splendid high-rate capability as shown in Figure 4d and Figure S6b. When increasing the current density to 500, 1000, and 2000 mA g^{-1}, high discharge capacities of 1100, 980, and 840 mA h g^{-1} can be delivered. Even when the current density is as high as 5000 mA g^{-1}, the RP@CNC anode can still show a high reversible capacity of 750 mA h g^{-1}. The GDC voltage profiles present very small potential hysteresis between discharge and charge curves in the RP@CNC anode, and the potential hysteresis is not obvious even under the high current density of 5000 mA g^{-1}, indicating the fast electrochemical kinetics of RP hosted in the CNCs. Figure S7a,b shows the sodium storage performance of CNCs, which shows a reversible capacity of only ∼150 mA h g^{-1} at 100 mA g^{-1} and negligible capacity at higher current density. The fast electrochemical kinetics of RP@CNCs is also demonstrated by the electrochemical impedance spectroscopy (EIS) analysis (Figure S8 and insert). The impedance plot comprises one semicircle at high-frequency, which is associated with the charge transfer resistance (R_{ct}) and impedance of Na-ion transport through the SEI film (R_{SEI}) and one sloping line at low frequency that corresponds to the diffusion of Na ion.[49] The data obtained from the equivalent circuit (Table S1) reveal that the R_{ct} and R_{SEI} of the RP@CNC electrode are 32.4 and 5.6 Ω, respectively. The favorable kinetics properties of RP@CNCs are associated with the high specific surface area and conductive carbon network.

Long-term cyclability is of vital importance to the practical application of NIBs. To determine the good cyclic stability, the RP@CNC composite was measured at a high current density of 5000 mA g^{-1} (Figure 4e). A high reversible capacity of 610
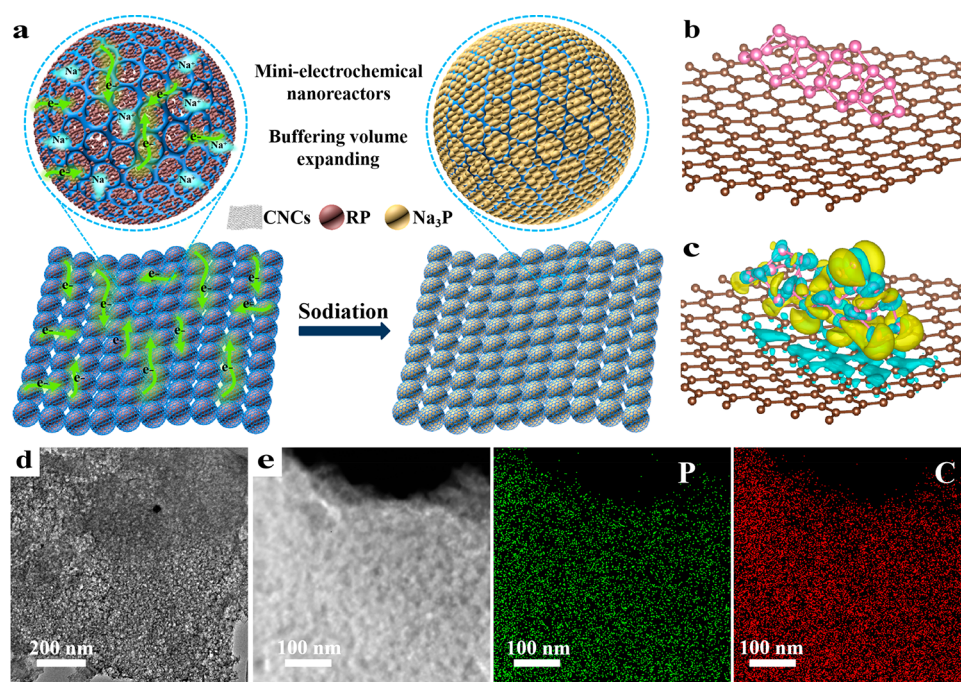
Figure 6. (a) Schematic diagram of electrochemically integrated circuit around the active mass and accommodation of volume expansion during sodiation process. DFT calculation showing (b) adsorption configuration of RP on graphitic layer, (c) charge density difference map of RP@CNC system, nudy blue and yellow regions represent the isosurfaces of electron depletion and accumulation, respectively. (d) TEM image and (e) elemental maps (C, P) for the RP@CNC anode cycled at 5000 mA g^{-1} after 1000 cycles.

mA h g^{-1} is delivered over 1300 loops with a high capacity retention of ∼80%, displaying a Coulombic efficiency stabilized at approximately 100% during the long-term period. The undulant capacity curves are due to the temperature fluctuation during testing.[23] These data confirm that the RP@CNC electrode is very competitive in capacity output as well as cycling stability. As compared with that of some previously reported RP based anodes (Figure 4f and Table S2),[7,8,12−31,49,50] the RP@CNC electrode delivers outstanding electrochemical performance for NIBs.

To interpret the high-rate capability of the RP@CNC composite, CV measurement at various sweep rates was performed to analysis the kinetics (Figure 5). Similar shapes are held with sweep rates increasing from 0.05 to 0.8 mV s^{-1}, and accordingly, the current intensity increases (Figure 5a). The equation $i = av^b$ can be used to evaluate the charge-storage mechanism, where b can be adjusted from 0.5 to 1.0 and calculated by fitting the slope of log(v) vs log(i). Correspondingly, a diffusion-controlled process is represented with a b value close to 0.5, while a capacitive-controlled behavior is indicated with a b value close to 1.[52,53] From Figure 5b, the b value of 0.73 can be quantified for anodic peak, suggesting the combination of the diffusion and capacitive controlled processes. Capacitive and diffusion contribution can be separated and quantified at a certain scan rate based on the equation $i = k_1 v + k_2 v^{1/2}$. For example, the capacitive contribution is quantified to be 59% at a scan rate of 0.2 mV s^{-1}, as shown in Figure 5c. The relative capacitive contributions at other scan rates of 0.05, 0.1, 0.4, and 0.8 mV s^{-1} are also determined to be 44%, 51%, 71%, and 90%, respectively (Figure 5d). The high capacitive contribution is indicative of faster kinetics reaction, thus leading to superior rate capability of RP@CNC anode.

The outstanding sodium storage properties of RP@CNCs can result from the porous and sheetlike structure, in which the amorphous RP is encapsulated in conductive and networked CNCs (Figure 6a). Specifically, the excellent electrical conductivity of the composite rendered by the conductive network feature of the carbon scaffold facilitates an efficient RP electrochemical utilization and fast reaction kinetics. The excellent electrical conductivity rendered by the conductive CNCs has been demonstrated by the DFT calculations. In the DFT calculations, the absorption and charge density distribution mainly result from the interface between RP and CNC; therefore, the bulk graphitic surface that is more relevant to the CNCs was simplified as a single graphene layer. As shown in Figure 6b,c, the interface between RP and carbon layers is the charge-accumulating regions, whereas the RP slab is the charge depletion regions, which suggest that the electric field directed from carbon layer to RP can be established. In addition, the interior cavities surrounded by thin low graphitized carbon shells serve as highly efficient mini-electrochemical nanoreactors and buffer the huge volume variation during cycling (Figure 6a),[40] thus guaranteeing excellent cycling stability. The fine accommodation of RP inside the CNCs hosts was demonstrated by the well-preserved original CNCs structure after 1000 cycles (Figure 6d), and the homogeneous distribution of RP within the CNCs hosts after the long-term cycles (Figure 6e). In addition, there are no characteristic peaks of RP in the XRD pattern of RP@CNCs after undergoing 1000 cycles (Figure S9), further demonstrating the good confinement of RP inside the CNCs hosts without exposed agglomeration of RP on the surface after cycling.

CONCLUSION

In summary, we have designed and fabricated a RP@CNC composite by encapsulating RP nanoparticles into the conductive and networked CNCs *via* a combination of a phosphorus-amine based method and evacuation-filling process. The controllable solution-based method and high surface CNC hosts not only ensure an ultrahigh RP loading amount of 85.3 wt % and effective RP utilization with a high reversible capacity of 1363 mA h g^{-1} after 150 cycles at 100 mA g^{-1} but also render excellent cycling stability within 1300 cycles with a very low capacity deterioration rate of 0.015% per cycle and high rate property (750 mA h g^{-1} at 5000 mA g^{-1}). The prepared RP based anode material has a broad prospect in the next-generation NIBs.

MATERIALS AND METHODS

Synthesis of RP@CNCs. The RP@CNC composite was obtained through the phosphorus-amine based method. On the basis of our previous work,[19] the RP-EN precursor solution was formed by adding 400 mg of commercial RP (Afla Aesar, 99%) into 20 mL of EN (Sigma, 99.5%) under stirring at 100 °C for 72 h. Then the RP-EN precursor solution was injected into 50 mg CNCs, synthesized according to the previous work,[34] under the conditions of evacuation and ultrasonication. With the addition of the deionized water into the above solution under the conditions of evacuation and ultrasonication, RP particles precipitated from the solution and encapsulated in the CNCs. To enhance the loading of RP, this process was repeated several times. Finally, the product was filtrated, rinsed, and freeze-dried. Detailed information about the material characterization, computational methods, and electrochemical measurements is supplied in the Supporting Information.

ASSOCIATED CONTENT

SI Supporting Information

The Supporting Information is available free of charge at https://pubs.acs.org/doi/10.1021/acsnano.1c00924.

Additional photos, SEM, TEM, XRD, Raman, electrochemical data; comparison of electrochemical performance; electrochemical impedance spectra (PDF)

AUTHOR INFORMATION

Corresponding Authors

Zheng Hu − *Department of Chemistry and Chemical Engineering, Nanjing University, Nanjing 210093, People's Republic of China;* ⬤ orcid.org/0000-0002-4847-899X; Email: zhenghu@nju.edu.cn

Xuebin Yu − *Department of Materials Science, Fudan University, Shanghai 200433, People's Republic of China;* ⬤ orcid.org/0000-0002-4035-0991; Email: yuxuebin@fudan.edu.cn

Authors

Weili Liu − *Department of Materials Science, Fudan University, Shanghai 200433, People's Republic of China*

Lingyu Du − *Department of Chemistry and Chemical Engineering, Nanjing University, Nanjing 210093, People's Republic of China*

Shunlong Ju − *Department of Materials Science, Fudan University, Shanghai 200433, People's Republic of China*

Xueyi Cheng − *Department of Chemistry and Chemical Engineering, Nanjing University, Nanjing 210093, People's Republic of China*

Qiang Wu − *Department of Chemistry and Chemical Engineering, Nanjing University, Nanjing 210093, People's Republic of China*

Complete contact information is available at:
https://pubs.acs.org/10.1021/acsnano.1c00924

Notes

The authors declare no competing financial interest.

REFERENCES

(1) Dunn, B.; Kamath, H.; Tarascon, J. M. Electrical Energy Storage for the Grid: A Battery of Choices. *Science* **2011**, *334*, 928−935.

(2) Kim, S.-W.; Seo, D.-H.; Ma, X.; Ceder, G.; Kang, K. Electrode Materials for Rechargeable Sodium-Ion Batteries: Potential Alternatives to Current Lithium-Ion Batteries. *Adv. Energy Mater.* **2012**, *2*, 710−721.

(3) Pan, H.; Hu, Y.-S.; Chen, L. Room-Temperature Stationary Sodium-Ion Batteries for Large-Scale Electric Energy Storage. *Energy Environ. Sci.* **2013**, *6*, 2338−2360.

(4) Berthelot, Y.; Carlier, D.; Delmas, C. Electrochemical Investigation of the P2-Na$_x$CoO$_2$ Phase Diagram. *Nat. Mater.* **2011**, *10*, 74−80.

(5) Yabuuchi, N.; Kajiyama, M.; Iwatate, J.; Nishikawa, H.; Hitomi, S.; Okuyama, R.; Usui, R.; Yamada, Y.; Komaba, S. P2-Type Na$_x$[Fe$_{1/2}$Mn$_{1/2}$]O$_2$ Made from Earth-Abundant Elements for Rechargeable Na Batteries. *Nat. Mater.* **2012**, *11*, 512−517.

(6) Wen, Y.; He, K.; Zhu, Y. J.; Han, F. D.; Xu, Y. H.; Matsuda, I.; Ishii, Y.; Cumings, J.; Wang, C. S. Expanded Graphite as Superior Anode for Sodium-Ion Batteries. *Nat. Commun.* **2014**, *5*, 4033.

(7) Qian, J.; Wu, X.; Cao, Y.; Ai, X.; Yang, H. High Capacity and Rate Capability of Amorphous Phosphorus for Sodium Ion Batteries. *Angew. Chem.* **2013**, *125*, 4731−4734.

(8) Kim, Y.; Park, Y.; Choi, A.; Choi, N.-S.; Kim, J.; Lee, J.; Ryu, J. H.; Oh, S. M.; Lee, K. T. An Amorphous Red Phosphorus/Carbon Composite as a Promising Anode Material for Sodium Ion Batteries. *Adv. Mater.* **2013**, *25*, 3045−3049.

(9) Fu, Y. Q.; Wei, Q. L.; Zhang, G. X.; Sun, S. H. Advanced Phosphorus-Based Materials for Lithium/Sodium-Ion Batteries: Recent Developments and Future Perspectives. *Adv. Energy Mater.* **2018**, *8*, 1702849.

(10) Han, X. P.; Han, J. P.; Liu, C.; Sun, J. Promise and Challenge of Phosphorus in Science, Technology, and Application. *Adv. Funct. Mater.* **2018**, *28*, 1803471.

(11) Liu, W. L.; Zhi, H. Q.; Yu, X. B. Recent Progress in Phosphorus Based Anode Materials for Lithium/Sodium Ion Batteries. *Energy Storage Mater.* **2019**, *16*, 290−322.

(12) Song, J. X.; Yu, Z. X.; Gordin, M. L.; Hu, S.; Yi, R.; Tang, D. H.; Walter, T.; Regula, M.; Choi, D.; Li, X. L.; Manivannan, A.; Wang, D. H. Chemically Bonded Phosphorus/Graphene Hybrid as a High Performance Anode for Sodium-Ion Batteries. *Nano Lett.* **2014**, *14*, 6329−6335.

(13) Zhang, C.; Wang, X.; Liang, Q.; Liu, X.; Weng, Q.; Liu, J.; Yang, Y.; Dai, Z.; Ding, K.; Bando, Y. Amorphous Phosphorus/Nitrogen-Doped Graphene Paper for Ultrastable Sodium-Ion Batteries. *Nano Lett.* **2016**, *16*, 2054−2060.

(14) Gao, H.; Zhou, T.; Zheng, Y.; Liu, Y.; Chen, J.; Liu, H.; Guo, Z. Integrated Carbon/Red Phosphorus/Graphene Aerogel 3D Architecture *via* Advanced Vapor-Redistribution for High-Energy Sodium-Ion Batteries. *Adv. Energy Mater.* **2016**, *6*, 1601037.

(15) Liu, Y. H.; Zhang, A. Y.; Shen, C. F.; Liu, Q. Z.; Cao, X.; Ma, Y. Q.; Chen, L.; Lau, C.; Chen, T.-C.; Wei, F.; Zhou, C. W. Red Phosphorus Nano-Dots on Reduced Graphene Oxide as a Flexible and Ultra-Fast Anode for Sodium-Ion Batteries. *ACS Nano* **2017**, *11*, 5530−5537.

(16) Liu, S.; Xu, H.; Bian, X. F.; Feng, J. K.; Liu, J.; Yang, Y. H.; Yuan, C.; An, Y. L.; Fan, R. H.; Ci, L. J. Nanoporous Red Phosphorus on Reduced Graphene Oxide as Superior Anode for Sodium-Ion Batteries. *ACS Nano* **2018**, *12*, 7380−7387.

(17) Pei, L. K.; Zhao, Q.; Chen, C. C.; Liang, J.; Chen, J. Phosphorus Nanoparticles Encapsulated in Graphene Scrolls as a High-Performance Anode for Sodium-Ion Batteries. *ChemElectroChem* **2015**, *2*, 1652−1655.

(18) Zeng, G.; Hu, X.; Zhou, B. L.; Chen, J. X.; Cao, C. S.; Wen, Z. H. Engineering Graphene with Red Phosphorus Quantum Dots for Superior Hybrid Anodes of Sodium-Ion Batteries. *Nanoscale* **2017**, *9*, 14722−14729.

(19) Liu, W. L.; Ju, S. L.; Yu, X. B. Phosphorus-Amine Based Synthesis of Nanoscale Red Phosphorus for Application to Sodium-Ion Batteries. *ACS Nano* **2020**, *14*, 974−984.

(20) Ruan, J. F.; Mo, F. J.; Long, Z. Y.; Song, Y.; Fang, F.; Sun, D. L.; Zheng, S. Y. Tailor-Made Gives the Best Fits: Superior Na/K-Ion Storage Performance in Exclusively Confined Red Phosphorus System. *ACS Nano* **2020**, *14*, 12222−12233.

(21) Song, J. X.; Yu, Z. X.; Gordin, M. L.; Li, X. L.; Peng, H. S.; Wang, D. H. Advanced Sodium-Ion Battery Anode Constructed *via* Chemical Bonding between Phosphorus, Carbon Nanotube and Crosslinked Polymer Binder. *ACS Nano* **2015**, *9*, 11933−11941.

(22) Wu, Y.; Xing, F. F.; Xu, R.; Cheng, X. L.; Li, D. J.; Zhou, X. F.; Zhang, Q. B.; Yu, Y. Spatially Confining and Chemically Bonding Amorphous Red Phosphorus in the Nitrogen Doped Porous Carbon Tubes Leading to Superior Sodium Storage Performance. *J. Mater. Chem. A* **2019**, *7*, 8581−8588.

(23) Liu, D.; Huang, X. K.; Qu, D. Y.; Zeng, D.; Wang, G. W.; Harris, J.; Si, J. Y.; Ding, T. Y.; Chen, J. H.; Qu, D. Y. Confined Phosphorus in Carbon Nanotube-Backboned Mesoporous Carbon as Superior Anode Material for Sodium/Potassium-Ion Batteries. *Nano Energy* **2018**, *52*, 1−10.

(24) Li, W. H.; Yang, Z. Z.; Li, M. S.; Jiang, Y.; Wei, X.; Zhong, X. W.; Gu, L.; Yu, Y. Amorphous Red Phosphorus Embedded in Highly Ordered Mesoporous Carbon with Superior Lithium and Sodium Storage Capacity. *Nano Lett.* **2016**, *16*, 1546−1553.

(25) Li, W. H.; Hu, S. H.; Luo, X. Y.; Li, Z. L.; Sun, X. Z.; Li, M. S.; Liu, F. F.; Yu, Y. Confined Amorphous Red Phosphorus in MOF-Derived *N*-Doped Microporous Carbon as a Superior Anode for Sodium-Ion Battery. *Adv. Mater.* **2017**, *29*, 1605820.

(26) Yao, S. S.; Cui, J.; Huang, J. Q.; Chong, W. G.; Qin, L.; Mai, Y. W.; Kim, J. K. Rational Assembly of Hollow Microporous Carbon Spheres as P Hosts for Long-Life Sodium-Ion Batteries. *Adv. Energy Mater.* **2018**, *8*, 1702267.

(27) Liu, B. Q.; Zhang, Q.; Li, L.; Jin, Z. H.; Wang, C. G.; Zhang, L. Y.; Su, Z. M. Encapsulating Red Phosphorus in Ultralarge Pore Volume Hierarchical Porous Carbon Nanospheres for Lithium/Sodium-Ion Half/Full Batteries. *ACS Nano* **2019**, *13*, 13513−13523.

(28) Sun, X. Z.; Li, W. H.; Zhong, X. W.; Yu, Y. Superior Sodium Storage in Phosphorus@Porous Multichannel Flexible Freestanding Carbon Nanofibers. *Energy Storage Mater.* **2017**, *9*, 112−118.

(29) Liu, Y. C.; Zhang, N.; Liu, X. B.; Chen, C. C.; Fan, L. Z.; Jiao, L. F. Red Phosphorus Nanoparticles Embedded in Porous *N*-Doped Carbon Nanofibers as High-Performance Anode for Sodium-Ion Batteries. *Energy Storage Mater.* **2017**, *9*, 170−178.

(30) Liu, Y. H.; Liu, Q. Z.; Jian, C.; Cui, D. Z.; Chen, M. R.; Li, Z.; Li, T.; Nilges, T.; He, K.; Jia, Z.; Zhou, C. W. Red-Phosphorus-Impregnated Carbon Nanofibers for Sodium-Ion Batteries and Liquefaction of Red Phosphorus. *Nat. Commun.* **2020**, *11*, 2520.

(31) Li, W. J.; Han, C.; Gu, Q. F.; Chou, S. L.; Liu, H. K.; Dou, S. X. Three-Dimensional Electronic Network Assisted by TiN Conductive Pillars and Chemical Adsorption to Boost the Electrochemical Performance of Red Phosphorus. *ACS Nano* **2020**, *14*, 4609−4617.

(32) Lyu, Z. Y.; Yang, L. J.; Xu, D.; Zhao, J.; Lai, H. W.; Jiang, Y. F.; Wu, Q.; Li, Y.; Wang, X. Z.; Hu, Z. Hierarchical Carbon Nanocages as High-Rate Anodes for Li- and Na-Ion Batteries. *Nano Res.* **2015**, *8*, 3535−3543.

(33) Wu, Q.; Yang, L. J.; Wang, X. Z.; Hu, Z. From Carbon-Based Nanotubes to Nanocages for Advanced Energy Conversion and Storage. *Acc. Chem. Res.* **2017**, *50*, 435−444.

(34) Xie, K.; Qin, X.; Wang, X.; Wang, Y.; Tao, H.; Wu, Q.; Yang, L.; Hu, Z. Carbon Nanocages as Supercapacitor Electrode Materials. *Adv. Mater.* **2012**, *24*, 347−352.

(35) Chen, S.; Bi, J. Y.; Zhao, Y.; Yang, L. J.; Zhang, C.; Ma, Y. W.; Wu, Q.; Wang, X. Z.; Hu, Z. Nitrogen-Doped Carbon Nanocages as Efficient Metal-Free Electrocatalysts for Oxygen Reduction Reaction. *Adv. Mater.* **2012**, *24*, 5593−5597.

(36) Lyu, Z. Y.; Xu, D.; Yang, L. J.; Che, R. C.; Feng, R.; Zhao, J.; Li, Y.; Wu, Q.; Wang, X. Z.; Hu, Z. Hierarchical Carbon Nanocages Confining High-Loading Sulfur for High-Rate Lithium-Sulfur Batteries. *Nano Energy* **2015**, *12*, 657−665.

(37) Zhang, Z. Q.; Chen, Y. G.; Zhou, L. Q.; Chen, C.; Han, Z.; Zhang, B. S.; Wu, Q. L.; Yang, J.; Du, L. Y.; Bu, Y. F.; Wang, P.; Wang, X. Z.; Yang, H.; Hu, Z. The Simplest Construction of Single-Site Catalysts by the Synergism of Micropore Trapping and Nitrogen Anchoring. *Nat. Commun.* **2019**, *10*, 1657.

(38) Shen, L. M.; Sun, T.; Zhuo, O.; Che, R. C.; Li, D. Q.; Ji, Y. C.; Bu, Y. F.; Wu, Q.; Yang, L. J.; Chen, Q.; Wang, X. Z.; Hu, Z. Alcohol-Tolerant Platinum Electrocatalyst for Oxygen Reduction by Encapsulating Platinum Nanoparticles inside Nitrogen-Doped Carbon Nanocages. *ACS Appl. Mater. Interfaces* **2016**, *8*, 16664−16669.

(39) Wu, Q.; Yang, L. J.; Wang, X. Z.; Hu, Z. Carbon-Based Nanocages: A New Platform for Advanced Energy Storage and Conversion. *Adv. Mater.* **2019**, *32*, 1904177.

(40) Liu, M.; Fan, H.; Zhuo, O.; Chen, J. C.; Wu, Q.; Yang, L. J.; Peng, L. M.; Wang, X. Z.; Che, R. C.; Hu, Z. A General Strategy to Construct Yolk-Shelled Metal Oxides inside Carbon Nanocages for High-Stable Lithium-Ion Battery Anodes. *Nano Energy* **2020**, *68*, 104368.

(41) Wu, Q.; Yang, L. J.; Wang, X. Z.; Hu, Z. Mesostructured Carbon-Based Nanocages: An Advanced Platform for Energy Chemistry. *Sci. China: Chem.* **2020**, *63*, 665−681.

(42) Li, D.; Kaner, R. B. Graphene-Based Materials. *Science* **2008**, *320*, 1170.

(43) Daasch, L.; Smith, D. A. Infrared Spectra of Phosphorus Compounds. *Anal. Chem.* **1951**, *23*, 853−868.

(44) Shi, Y.; Belosinschi, D.; Brouillette, F.; Belfkira, A.; Chabot, B. Phosphorylation of Kraft Fibers with Phosphate Esters. *Carbohydr. Polym.* **2014**, *106*, 121−127.

(45) Fuente, E.; Menéndez, J. A.; Díez, M. A.; Suárez, D.; Montes-Morán, M. A. Infrared Spectroscopy of Carbon Materials: A Quantum Chemical Study of Model Compounds. *J. Phys. Chem. B* **2003**, *107*, 6350−6359.

(46) Perez-Romo, P.; Potvin, C.; Manoli, J. M.; Chehimi, M. M.; Djega-Mariadassou, G. J. Phosphorus-Doped Molybdenum Oxy-Nitrides and Oxygen-Modified Molybdenum Carbides: Synthesis, Characterization, and Determination of Turnover Rates for Propene Hydrogenation. *J. Catal.* **2002**, *208*, 187−196.

(47) Watanabe, J.; Nederberg, F.; Atthoff, B.; Bowden, T.; Hilborn, J.; Ishihara, K. Cytocompatible Biointerface on Poly(Lactic Acid) by Enrichment with Phosphorylcholine Groups for Cell Engineering. *Mater. Sci. Eng., C* **2007**, *27*, 227−231.

(48) Watanabe, J.; Ishihara, K. Change in Cell Adhesion Property on Cytocompatible Interface Using Phospholipid Polymer Grafted with Poly(d, l-Lactic Acid) Segment for Tissue Engineering. *Sci. Technol. Adv. Mater.* **2003**, *4*, 539−544.

(49) Liu, S.; Feng, J. K.; Bian, X. F.; Liu, J.; Xu, H.; An, Y. L. A Controlled Red Phosphorus@Ni-P Core@Shell Nanostructure as an Ultralong Cycle-Life and Superior High-Rate Anode for Sodium-Ion Batteries. *Energy Environ. Sci.* **2017**, *10*, 1222−1233.

(50) Liu, W. L.; Yuan, X. X.; Yu, X. B. A Core-Shell Structure of Polydopamine-Coated Phosphorus-Carbon Nanotube Composite for

High-Performance Sodium-Ion Batteries. *Nanoscale* **2018**, *10*, 16675−16682.

(51) Liu, Y.; Fang, Y. J.; Zhao, Z. W.; Yuan, C. Z.; Lou, X. W. A Ternary $Fe_{1-x}S$@Porous Carbon Nanowires/Reduced Graphene Oxide Hybrid Film Electrode with Superior Volumetric and Gravimetric Capacities for Flexible Sodium Ion Batteries. *Adv. Energy Mater.* **2019**, *9*, 1803052.

(52) Brezesinski, T.; Wang, J.; Tolbert, S. H.; Dunn, B. Ordered Mesoporous α-MoO_3 with Iso-oriented Nanocrystalline Walls for Thin-Film Pseudocapacitors. *Nat. Mater.* **2010**, *9*, 146−151.

(53) Zhao, C.; Yu, C.; Zhang, M.; Huang, H.; Li, S.; Han, X.; Liu, Z.; Yang, J.; Xiao, W.; Liang, J.; Sun, X.; Qiu, J. Ultrafine MoO_2-Carbon Microstructures Enable Ultralong-Life Power-Type Sodium Ion Storage by Enhanced Pseudocapacitance. *Adv. Energy Mater.* **2017**, 71602880.